Insight in NO synthesis in a gliding arc plasma via gas temperature and density mapping by laser-induced fluorescence

Filippo Manaigo[a,b,†], Abhyuday Chatterjee[a], Annemie Bogaerts[b], and Rony Snyders[a,c]

[a]Research Group ChIPS, Department of Chemistry, University of Mons, Place du Parc 20, 7000 Mons, Belgium
[b]Research Group PLASMANT, Department of Chemistry, University of Antwerp, Universiteitsplein 1, 2610 Antwerp, Belgium
[c]Materia Nova Research Center, Parc Initialis, 7000 Mons, Belgium
[†]Corresponding author: filippo.manaigo@umons.ac.be

Abstract

A gliding arc plasma, operating at atmospheric pressure in a gas mixture of 50 % N_2 and 50 % O_2, is studied using laser-induced fluorescence spectroscopy. The main goal is to determine the two-dimensional distribution of both the gas temperature and the NO ground state density in the afterglow. As gliding arc plasma discharges at atmospheric pressure normally produce rather high NO_x densities, the high concentration of relevant absorbers, such as NO, may impose essential restrictions for the use of "classical" laser-induced fluorescence methods (dealing with excitation in the bandhead vicinity), as the laser beam would be strongly absorbed along its propagation in the afterglow. Since this was indeed the case for the studied discharge, an approach dealing with laser-based excitation of separate rotational lines is proposed. In this case, due to a non-saturated absorption regime, simultaneous and reliable measurements of both the NO density and the gas temperature (using a reference fitting spectrum) are possible. The proposed method is applied to provide a two-dimensional map for both the NO density and the gas temperature at different plasma conditions. The results show that the input gas flow rate strongly alters the plasma shape, which appears as an elongated column at low input gas flow rate and spreads laterally as the flow rate increases. Finally, based on temperature map analysis, a clear correlation between the gas temperature and NO concentration is found. The proposed method may be interesting for the plasma-chemical analysis of discharges with high molecular production yields, where knowledge of both molecular concentration and gas temperature is required.

1 Introduction

The process of converting stable nitrogen molecules (N_2) into more reactive N-containing compounds, such as nitric oxide (NO), nitrogen dioxide (NO_2), ammonia (NH_3), etc. is known as nitrogen fixation. Compared to N_2, these compounds have weaker chemical bonds, thus, allowing for atomic nitrogen (N) to be easily accessible to living organisms. This process is particularly relevant in agriculture, as the production of nitrogen-containing fertilizers is responsible for most of the demand for nitrogen compounds, registering in 2019 a consumption of 107 million tons of N [1]. Nowadays, such demand for nitrogen compounds is met with the Haber-Bosch (H-B) process [2], which consists of the catalytic synthesis of NH_3. Due to the high temperatures (650 K - 750 K) and pressures (100 bars) required, the H-B process greatly benefits from economies of scale and, thus, is mainly performed in large and centralized facilities [3, 4]. Despite its good energy efficiency, the H-B process is estimated to be responsible for approximately 1% of the world energy consumption and 1% of the CO_2 emissions in 2019 [5, 6], making a rather urgent need for the development of a "greener" alternative for nitrogen fixation, which could reduce the energy consumption and the carbon footprint.

In this framework, it has been suggested that the theoretical limit of the energy cost for plasma-based nitrogen fixation into NO is lower than what is theoretically achievable with the H-B process, i.e., 0.35 MJ/mol. [3]. This is possible through the Zeldovich mechanism, where N_2 molecules react with atomic oxygen (O) and form NO:

$$N_2(g, v) + O \rightarrow NO + N \tag{1}$$

where g and v indicate the ground state and a vibrationally excited state, respectively. As stated, the Zeldovich reaction can occur from both N_2(g) and N_2(v). In the first case, it is defined as the thermal Zeldovich mechanism, while in the second case, it is called the "vibrationally-enhanced Zeldovich mechanism" [7]. In warm plasmas, such as the GAP, the dominant process is expected to be the thermal Zeldovich mechanism because of the high gas temperature of several 1000 K. The produced N atom can then further react with O_2, also leading to NO production:

$$O_2 + N \longrightarrow NO + O. \tag{2}$$

Part of the produced NO can be either lost through the Zeldovich back reaction (i.e. the opposite reaction of equations (1) and (2)) or be further oxidized, forming NO_2:

$$2\,NO + O_2 \longrightarrow 2\,NO_2. \tag{3}$$

$$NO + O \longrightarrow NO_2 \tag{4}$$

Gliding arc (GA) plasmas are considered a promising alternative to the H-B process for nitrogen fixation. The main advantages of GA plasmas consist in the possibility of operating them at atmospheric pressure, allowing for relatively easy industrial implementation, and in the generation of a reduced electric field below 100 Td, which is beneficial for nitrogen oxidation as it favors vibrational excitation over more energetic processes such as electronic excitation or ionization [8]. On the other hand, the Zeldovich mechanism for NO formation mainly proceeds thermally in GA plasmas, because the high gas temperature yields pronounced vibrational-translational relaxation, causing gas heating and

depopulation of the vibrational levels. Nevertheless, this thermal mechanism is also quite efficient, due to the high temperatures, and explains the good energy efficiency for nitrogen fixation [8].

Today, the best performance obtained with a gliding arc plasmatron (GAP) consists of a maximum NO_x yield of 1.5 % at an energy cost of 3.6 MJ/mol [7]. More success has been achieved with rotating gliding arc (RGA) plasmas, whose main difference from the GAP consists in the shape of its electrodes: in this case, a cone-shaped cathode is placed in a hollow anode. Such modification ensures that a higher fraction of the gas interacts with the arc, which is beneficial to improve the reactor performance [9]. Considering a RGA, a 6 % NO_x yield with a 2.1 MJ/mol energy cost was obtained with the introduction of an effusion nozzle, used to lower the gas temperature immediately after the plasma and prevent the dissociation of NO into N_2 and O_2 [10]. On the other hand, by increasing the pressure in such a reactor up to 4 bar the overall equilibrium NO concentration increases, and the rate of equation (4) becomes dominant over the Zeldovich back-reaction. This results in a yield up to 4.8 % with an energy cost down to 1.8 MJ/mol [11]. The main tool for the interpretation of these results, both for GAP and RGA plasmas, is the use of simulations to model the vibrational and gas temperatures and species concentration (NO, NO_2, N, O) in the active region of the plasma [7, 10, 12, 13]. More specifically, a kinetic model proposed in [7] shows the time evolution of the number densities of NO, NO_2, N and O in the GAP operating with N_2 and O_2, but the experimental benchmark was limited to the final NO_x yield and energy cost [7]. Hence, there is a strong need to experimentally determine the plasma species densities and gas temperature to support these modelling results.

Laser-induced fluorescence (LIF), as a diagnostic method for NO-containing plasmas, is widely used for low-pressure plasmas [14, 15], atmospheric pulsed plasmas [16] or, more in general, when small (up to few tens of ppm) concentrations of NO are involved [17, 18]. Generally in literature, NO bandheads corresponding to high absorption are measured to maximise the LIF signal intensity. This, however, is not possible at the conditions under study here due to the effect of the high density of the absorber (NO) on the intensity of the laser beam. Indeed, if set at the wavelength of one of the main NO bandheads, the laser beam is poorly detectable after passing the plasma volume. The LIF radiation corresponding to such conditions, if detectable, is characterized by a high non-uniformity along the propagation axis of the laser beam and is generally characterized by a weak intensity. And yet, the measurement of the beam energy (or of its intensity) is crucial in order to compare different LIF signals and to build a LIF line profile. Thus, in order to be able to map the species of interest when the absorption is too high, one may consider working with an optical transition corresponding to a weak absorption coefficient [16].

For this reason, this work focuses on providing and testing an alternative LIF-based method that could be suitable for plasmas with a high density of absorbers.

This method is then used to determine the spatial distribution of the gas temperature and NO concentration in the afterglow of the plasma, i.e., a few mm below the arc in a GAP used for NF and to evaluate the impact of the experimental parameters on these features. The study of the afterglow can prove to be important to gain more insight into possible back-reactions,

and to study quenching effects. To get a complete picture of the process, the concentration measurements are compared with the gas composition at the exhaust as measured by Fourier transform infrared (FTIR) spectroscopy.

2 Setup

2.1 Gliding Arc Reactor

The schematics of the GAP are shown in figure 1a. A DC power supply (Technix SR12KV-15KW) is connected, through a 4 kΩ resistor, to the GAP cathode. The power supply had a negative polarity and it could provide an output voltage and current up to 12 kV and 1.25 A, respectively. As for the experimental measurements the current was set to either 150 mA, 200 mA or 250 mA. The typical duration of the arc is of the order of a few ms. The anode was directly connected to the main body of the reactor, which was grounded. A detailed representation of the stainless steel electrodes can be found in figure 1b. The two electrodes were separated by a 2 mm gap and a Teflon fit ensured that the cathode was electrically insulated from the main body of the reactor. The inner diameters of the cathode and the anode were 17.5 mm and 14.2 mm, respectively. This ensured that the gas, which was tangentially injected between the electrodes, could operate in the reverse vortex flow (RVF) regime. This configuration has been proven to ensure better confinement of the arc in the center of the electrodes, enhancing the heat insulation and the fraction of gas flowing into the arc [19, 20]. The GAP reactor was operated at atmospheric pressure with a gas mixture of 50 % N_2 and 50 % O_2. Two different total flow rates of 8 and 10 standard liters per minute (slm) were used. The main body of the reactor was cooled with a 20 cm diameter industrial fan. The top of the main body of the reactor was equipped with four quartz windows. The reactor exhaust is connected to an external gas cell where the NO_x concentrations are measured with a Vertex 80v FTIR spectrometer by Bruker. The internal RT-DLaTGS (Deuterated Lanthanum α-alanine-doped Triglycine Sulfate) detector in the mid-IR region is used for absorbance measurement. The gas cell length is approximately 125 mm and is equipped with two Si windows. A 2 mm aperture is used, which gives a resolution of 1 cm^{-1}. For each measurement, 20 spectra acquired in the range between 1000 cm^{-1} and 3500 cm^{-1} were averaged.

2.2 LIF Setup

A Nd:YAG (neodymium-doped yttrium aluminum garnet) laser working at 355nm with a 10 Hz repetition rate pumped a solution of Coumarin 2 dye in methanol. The beam was generated in pulses with a Gaussian profile in time with a 5 ns full width at half maximum. The Sirah Cobra Stretch dye laser was equipped with a second harmonic generation unit, resulting in a wavelength that could be tuned between approximately 217 nm and 231 nm. Before being injected into the plasma, the beam was collimated with a f/50cm lens. The LIF emission from the plasma afterglow was collected with an Andor iStar 740 Intensified Charge-Coupled Device (ICCD) camera equipped with a CERCO UV f/100cm lens and a (248 ± 10) nm bandfilter. The ICCD was placed in the z direction (perpendicularly with respect to the laser beam path) and synchronized with the laser using a DG645 digital delay generator. The x and y directions are defined as the horizontal position (which is parallel to the beam path) and the distance from

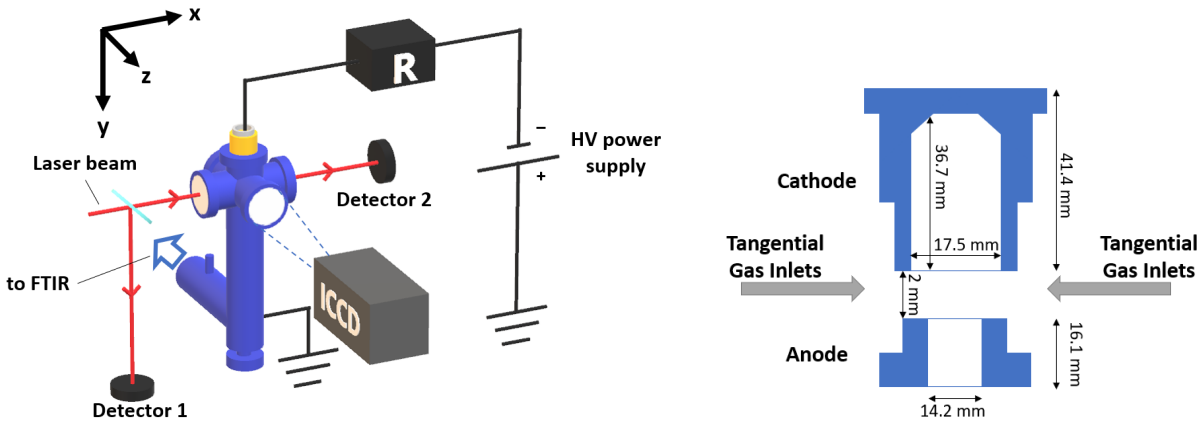

(a) (b)

Figure 1: Scheme of the experimental setup highlighting the electrical circuit and the laser beam path, which probes the plasma afterglow, (a) and of the electrodes, located inside the highlighted yellow cylinder, for which the most significant dimensions are shown (b). As a reference, the axes used in figure 2 are highlighted. A 4 kΩ resistance (R) was placed between the GAP cathode and the power supply.

the anode, respectively.

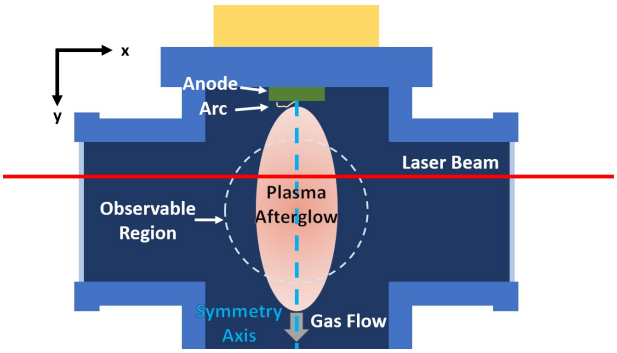

Figure 2: Cross section of the GAP system, seen from the ICCD, showing the region of the plasma afterglow. The region where LIF could be observed is shown with a white circular dashed line.

A small part of the initial laser beam was redirected toward an Ophir PE-9 energy meter head ("detector 1"). A second identical energy meter head ("detector 2"), also used as a beam dump, was used to measure the beam energy after passing the plasma afterglow. Due to the reactor design, the region that could be probed with LIF was limited and depended on the size of the quartz windows as schematized in figure 2. This allowed the plasma afterglow to be optically probed in the distance range (from the anode) of 10 and 40 mm and prevented the electric arcs from being observable with the camera. Near the anode (i.e., GAP reactor outlet) a small arc is drawn, which is typically observed just a few mm outside the GAP [19, 21]. A known gas mixture of 1 % NO in Ar was available for calibration.

3 LIF methodology implementation

3.1 Temperature measurements

The region near the band head of the NO(X, $v = 0$) $\rightarrow$ NO(A, $v = 0$) transition was avoided due to a strong laser absorption causing the absorption signal to scale non-linearly with the absorber density. Therefore, LIF was performed with the wavelengths around the two peaks observed at 224.792 nm and at 224.823 nm where the absorbance was lower, allowing the laser energy to be detectable at detector 2 and, thus, to estimate the beam energy. With this configuration, the J = 33.5 (Q-branch) and the J = 21.5 (R-branch) rotational lines of the transition NO(X, $v = 0$) $\rightarrow$ NO(A, $v = 0$) could be, respectively excited. The NO then de-excited to, among many other levels, the NO(X, $v = 2$) state corresponding to a rotational band with a bandhead at about 248 nm. In this work, this line ratio demonstrated high T_{gas} sensitivity, along with a linear absorption regime and a clearly detectable laser beam energy at detector 2 and, therefore, it was chosen for T_{gas} measurements. A NO LIF spectrum simulated to LIFBASE is shown in figure 3 as a reference. The J = 33.5 and the J = 21.5 transition are highlighted.

Figure 4 shows an example of the LIF image captured with the camera. The axes represent the horizontal position and the distance in the afterglow, measured from the anode (as shown in figure 2) expressed in mm. To study the evolution of the LIF signal along the laser beam, the region corresponding to the beam path was horizontally subdivided into smaller integration areas where the LIF signal was analyzed separately. In general, the LIF signal intensity (I_{LIF}) corresponding to the laser-induced excitation from state j to i and the consequent de-excitation from state i to k can be expressed as follows [22]:

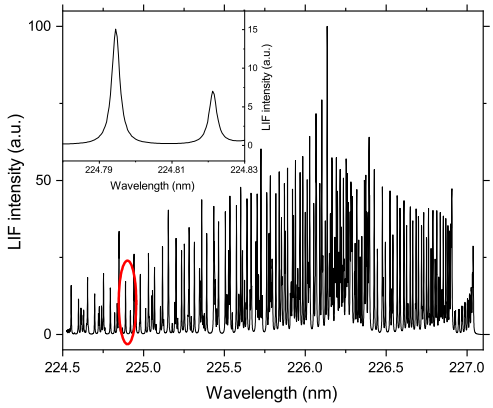

Figure 3: LIF NO signal simulated with LIFBASE with $T_{vib} = T_{rot} = 1000$K

$$I_{LIF} = C n_j E_{las} \frac{A_{ik} B_{ji}}{Q_i + \sum_l A_{il}}, \tag{5}$$

where C is a constant, n_j is the density of the state j, E_{las} is the energy of the laser pulse, A_{ik} and B_{ji} are the Einstein emission and absorption coefficients, respectively, A_{il} is the Einstein emission coefficient from state i to a generic state l and Q_i is the collisional quenching rate. Equation (5) represents a linear regime when fluorescence intensity scales with the laser energy. An example of the LIF intensity spectrum, and the fit evaluated with LIFBASE, a free spectroscopy software, in the vicinity of $J = 33.5$ and $J = 21.5$ NO(X, $v = 0$) lines is shown in figure 5 together with the line absorption (A_L), evaluated as [23]

$$A_L = 1 - \frac{I^f_{las}}{I^0_{las}} = 1 - \frac{E^f_{las}}{E^0_{las}} \tag{6}$$

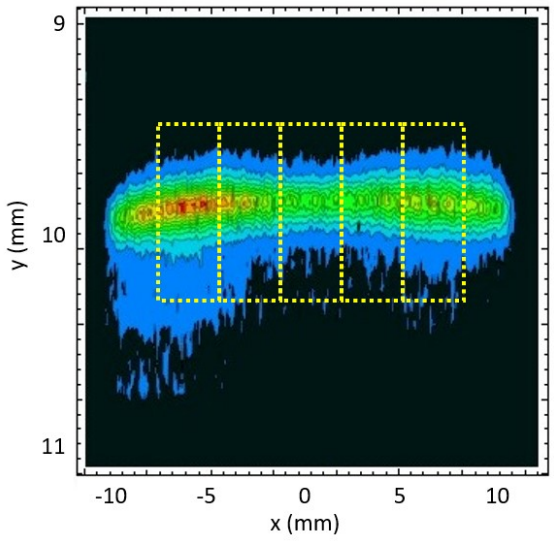

Figure 4: Example of a LIF signal measured. The beam path region was subdivided into smaller integration areas highlighted with the dashed boxes. The current was set at 150 mA and the input gas flow rate at 10 slm. The laser beam propagates from left to right.

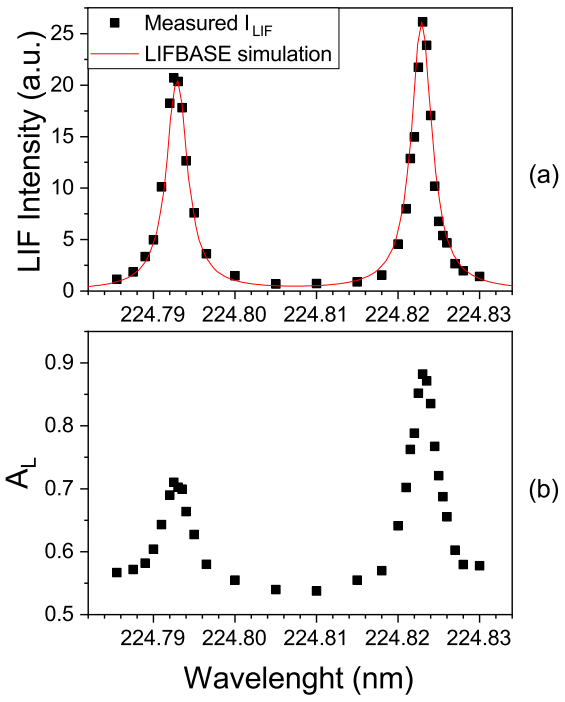

Figure 5: Intensity of the LIF signal (a) and laser beam line absorption A_L (b) as a function of the laser beam wavelength. The current was set at 150 mA and the input gas flow rate at 10 slm. The LIF intensity spectrum simulated with LIFBASE (T_{gas} = 640 K) is shown in red.

where I_{las} is the initial laser intensity and the indexes 0 and f refer to the quantity being measured before (with detector 1) and after (with detector 2) passing through the probed region, respectively. Since the laser frequency and the pulse duration were constant, A_L can be evaluated using the laser energy. As shown in figure 5, the laser line absorption values in this work are high and, typically, between 0.5 to 0.9. A high A_L was observed between the $J = 33.5$ and the $J = 21.5$ absorption peaks but did not result in a photon emission around 248nm (the LIF intensity in figure 5(a) between the two peaks is close to zero). This could be caused by the presence of NO_2, also produced in the GAP, which is known to have a non-negligible and continuous absorption spectrum around 224nm, which results in emission at different wavelengths compared to NO [24].

Due to the high laser absorbance, the energy of the laser in equation (5) could not be assumed constant along the absorption path. Additionally, the evolution of the beam energy profile was affected by the NO density profile, which, as discussed in section 4 in terms of concentration, greatly varied for different initial conditions. To

still be able to restore the laser energy in the point of interest (middle of the discharge), considering the geometry of the electrodes and the reactor, a cylindrical symmetry for both the gas temperature and species density in the discharge volume was assumed. In figure 2 the symmetry axis, corresponding to the center of the anode and, thus, of the reactor, is marked with a vertical light blue dashed line. The horizontal position is centered on the symmetry axis. With this assumption, the symmetry axis separates the laser beam path into two sections characterized by the same length and the same NO concentration (which is not uniform, but equal between the two regions), thus allowing the laser beam intensity at the center of the GAP to be evaluated with the Beer-Lambert law. If L is the optical length of the GAP and c is the average NO concentration, from the general equation, the laser intensities measured at detector 2 $I_{las}(L)$ and at the center $I_{las}(L/2)$ are

$$I_{las}(L) = I^0_{las} e^{-\epsilon c L}, \tag{7}$$

$$I_{las}(L/2) = I^0_{las} e^{-\epsilon c \frac{L}{2}}, \tag{8}$$

where ϵ is the molar absorption coefficient. By multiplying equation (7) by I^0_{las}, the relation between $I_{las}(L/2)$ and the measurable laser intensities I^0_{las} and $I_{las}(L)$ becomes

$$I_{las}(L) \cdot I^0_{las} = I^0_{las} I^0_{las} e^{-\epsilon c L} = \left(I_{las}(L/2)\right)^2 \tag{9}$$

since the laser intensity and the laser energy are linearly dependent, the energy of the beam at the center of the GAP can be expressed as

$$E_{las}(L/2) = (E^0_{las} E_{las}(L))^{\frac{1}{2}}. \tag{10}$$

The LIF spectra, as the one shown in figure 4, were then integrated and normalized to $E_{las}(L/2)$. For each experimental condition, the laser beam wavelength was scanned between 224.785 nm and 224.830 nm, as shown in figure 5(a).

It should be noted that using $E_{las}(L/2)$ to normalize the LIF signal from an integration area that is not centered in the symmetry axis is a simplification. The inaccuracies caused by this approach are corrected by imposing the symmetry hypothesis previously discussed and averaging the T_{rot} and NO density calculated from integration areas with the same distance from the symmetry axis. The peaks of the LIF intensities followed a Lorentz distribution, which is usually associated with collisional broadening, which becomes dominant at atmospheric pressure [25].

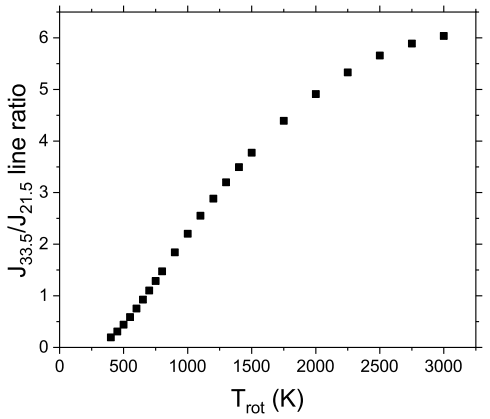

Figure 6: $J_{33.5}/J_{21.5}$ line ratio, simulated with LIFBASE software, as a function of T_{rot}.

The 224.792 nm and 224.823 nm ($J_{33.5}/J_{21.5}$) line ratio showed a rather high sensitivity to T_{rot}. Its evolution was simulated with LIFBASE 2.1.1 software [26] and is shown in figure 6. For this reason, the $J_{33.5}/J_{21.5}$ line ratio was used to evaluate the T_{rot} of NO(X, $v = 0$). As the rotational-

translational relaxation is estimated to be in the ns range [27], much shorter than the duration of the arc and the time the gas requires to reach the probed region, both of the order of a few ms [20], T_{rot} is assumed to be equal to the gas temperature T_{gas}. As shown in figure 5, the absorption for the J=21.5 peak is higher. Thus, the approximation introduced with the use of $E_{las}(L/2)$ for the normalization of the LIF signal causes T_{rot} to be higher on the left-hand side of the symmetry axis (where the laser beam enters the probed region). This difference increases with the distance from the symmetry axis and, at the extremes, is typically of the order of 10-15% of the measured T_{rot}. To correct this difference, the measured T_{rot} were then adjusted to impose the cylindrical symmetry by averaging the two points at the same distance from the symmetry axis.

3.2 Density measurements

For the density determination, the $J = 21.5$ peak (at 224.823 nm) was taken due to the I_{LIF} intensity of the $J = 33.5$ peak being too low in the calibration spectra. The density n_j at the center of the reactor can be extracted from equation (5):

$$n_j \propto \frac{I_{LIF}}{E_{las}(L/2)} \frac{1}{\tau}, \tag{11}$$

where j corresponds to the NO($X, v = 0, J = 21.5$) state and τ is the decay time (whose measurement is discussed in section 3.3) defined as:

$$\tau = (Q_i + \sum_l A_{il})^{-1}. \tag{12}$$

n_j can be obtained by comparison with the I_{LIF} from the calibration gas mixture. Considering equation (11) for both the measurements and the calibration, the relation between n_j and the NO($X, v = 0, J = 21.5$) density of the calibration gas ($n_{j,cal}$) becomes:

$$n_j = n_{j,cal} \frac{I_{LIF}}{E_{las}(L/2)} \frac{E_{las,cal}(L/2)}{I_{LIF,cal}} \frac{\tau_{cal}}{\tau}, \tag{13}$$

where the index *cal* refers to the quantities relative to the calibration gas mixture. The fraction of the NO(X) molecules in the NO($X, v = 0, J = 21.5$) state is described by the vibrational and rotational statistical factor $\Phi_{J=21.5}$ and $\Phi_{v=0}$, respectively, which depend on T_{gas}. Thus, in order to link n_j with the NO(X) density (n_{NO}), an additional correction is required.

$$n_{NO} = n_{NO,cal} \frac{\Phi_{J=21.5,cal}}{\Phi_{J=21.5}} \frac{\Phi_{v=0,cal}}{\Phi_{v=0}} \cdot \frac{n_j}{n_{j,cal}}, \tag{14}$$

where both $\Phi_{J=21.5}$ and $\Phi_{v=0}$ are normalized ($\sum_J \Phi_J = \sum_v \Phi_v = 1$). The statistical factors were simulated with LIFBASE [26], using the T_{rot} measured by LIF. Considering the pressure and T_{gas} in the GAP, the vibrational-translational relaxation time is estimated to have the order of magnitude of a few μs [27, 28]. As, both the time required by the gas to reach the probed region and the typical duration of the arc is of the order of a few ms, $T_{vib} = T_{rot}$ is assumed for the evaluation of $\Phi_{v=0}$. This is a reasonable assumption as, in atmospheric pressure GAPs, T_{vib} and T_{rot} are generally considered in equilibrium [8].

Finally, as in this work, rather than n_{NO}, the NO(X) concentration (c_{NO}) is used, an additional correction is introduced using the ideal gas law.

$$c_{NO} = c_{NO,cal} \frac{T_{gas}}{T_{gas,cal}} \cdot \frac{n_{NO}}{n_{NO,cal}} \tag{15}$$

where $c_{NO,cal}$ is the NO(X) concentration of the calibration gas mixture, which is known.

3.3 LIF effective decay time

Table 1: Parameters of the fit shown in figure 7.

	slope (ns^{-1}/Ar%)	y-intercept (ns^{-1})
J=33.5	$-(3.28 \pm 0.08) \cdot 10^{-3}$	0.333 ± 0.007
J=21.5	$-(3.2 \pm 0.2) \cdot 10^{-3}$	0.32 ± 0.02

The effective decay time, τ, is a crucial parameter for the calibration. As a consequence of equation (11), its measurement is required to determine n_j, and thus c_{NO}. While for the calibration gas mixture (NO in Ar), the measurement of τ_{cal} is relatively simple, it can prove to be more challenging when plasmas at atmospheric pressure are involved since τ can be comparable to or shorter than the laser pulse duration.

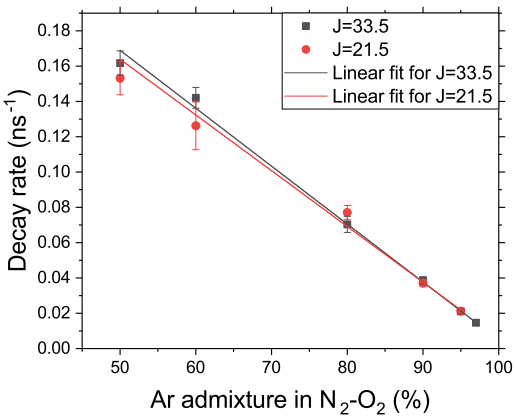

Figure 7: Decay rate of NO($X, v = 0, J = 33.5$) (224.792 nm) and NO($X, v = 0, J = 21.5$) (224.792 nm) excited states as a function of the Ar percentage of the N_2-O_2 input gas mixture.

With the studied gas composition, O_2 is known to be the main quencher for NO, showing a negligible dependency on T_{gas} [29]. In this work, τ was measured by diluting the input gas flow rate of N_2 and O_2 with Ar, a relatively weak quencher. This allowed to keep τ in the ns range and measure it directly with the 5 ns pulsed dye laser [30, 31]. More specifically, it has been shown that the NO(A) decay rate, defined as τ^{-1} decreases linearly as the Ar concentration increases [32]. Figure 7 shows the evolution of τ^{-1} as the Ar fraction increases for both the fluorescence lines. The total input gas flow rate was kept at 10 slm, the current at 150 mA and the beam distance from the anode was set at 10 mm. The measurements were fitted with a straight line, whose parameters are listed in table 1. From the y-intercept of the fit, τ associated to the $J = 33.5$ and $J = 21.5$ states is estimated to be (3.00 ± 0.07) ns and (3.1 ± 0.2) ns, respectively.

As previously mentioned, for the calibration gas mixture a direct measure of the decay time, $\tau_{cal} = 102$ ns, was possible.

3.4 Self-absorption

With a high density of absorbers, self-absorption, i.e. the absorption in the plasma of the fluorescence light, can lower the measured I_{LIF}. Since the fluorescence emission is in the NO($A, v = 0$) $\rightarrow$ NO($X, v = 2$) band, a significant NO($X, v = 2$) population would be required to have a noticeable self-absorption effect, which is not the case in a warm plasma such as a GAP.

More generally, a critical NO ground state density for self-absorption to become non-negligible is reported to be 2×10^{17} cm^{-3} [33]. In this work, as described in section 4, the highest n_{NO} is obtained for 8 slm and 250 mA, where a c_{NO} and T_{gas} of 1.2 % and 610 K is measured, respectively. Using the ideal gas law, this corresponds to a n_{NO} of approximately

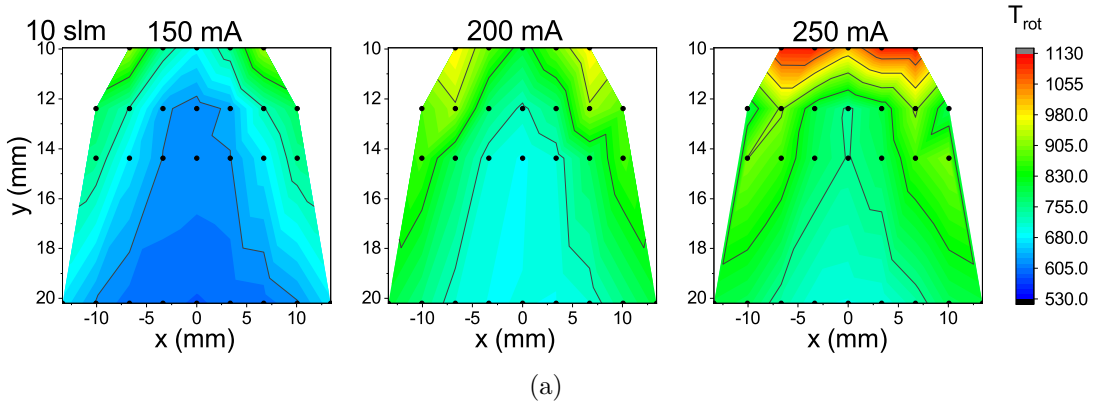

(a)

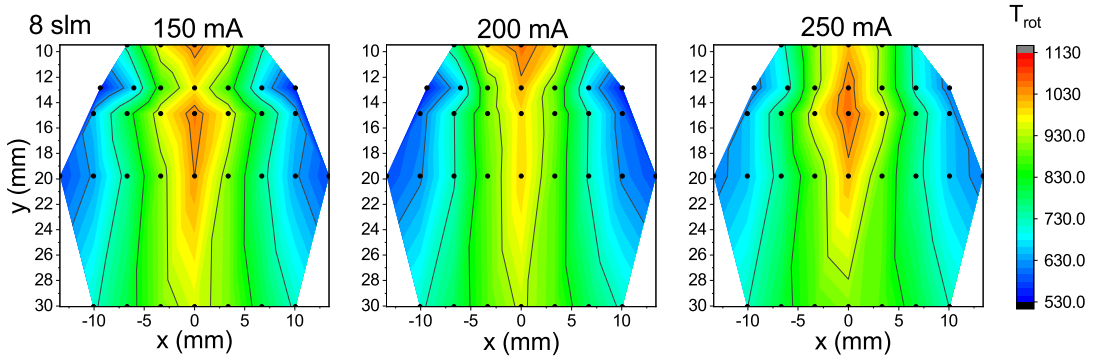

(b)

Figure 8: 2D vertical section of the T_{rot} distribution in the plasma afterglow at 10 slm (a) and 8 slm (b) with currents of either 150 mA, 200 mA or 250 mA. The data points are highlighted.

1.4×10^{17} cm^{-3}. Overall, n_{NO} is measured to be in the range between 3.5×10^{16} cm^{-3} and 1.4×10^{17} cm^{-3}, which is lower than the critical NO density, allowing to neglect the effects of self-absorption in this work.

4 Process evaluation

The 2D temperature maps in the plasma afterglow for different discharge conditions show spatial non-uniformity. This can be observed in figures 8a and 8b, which show the spatial evolution of the T_{rot} distribution for NO(X,$v = 0$) for two different input gas flow rates of 8 slm and 10 slm with the same composition (50% N_2 + 50% O_2). As mentioned in section 2.2, the y-axis measures the vertical distance in the afterglow, measured from the anode (reactor outlet) and the x-axis represents the horizontal position i.e. the distance from the center.

It is observed that the difference in the temperature distribution between the two measurement sets of 8 slm and 10 slm correlates with the different plasma shapes. A higher input gas flow rate pushes the plasma radially, causing it

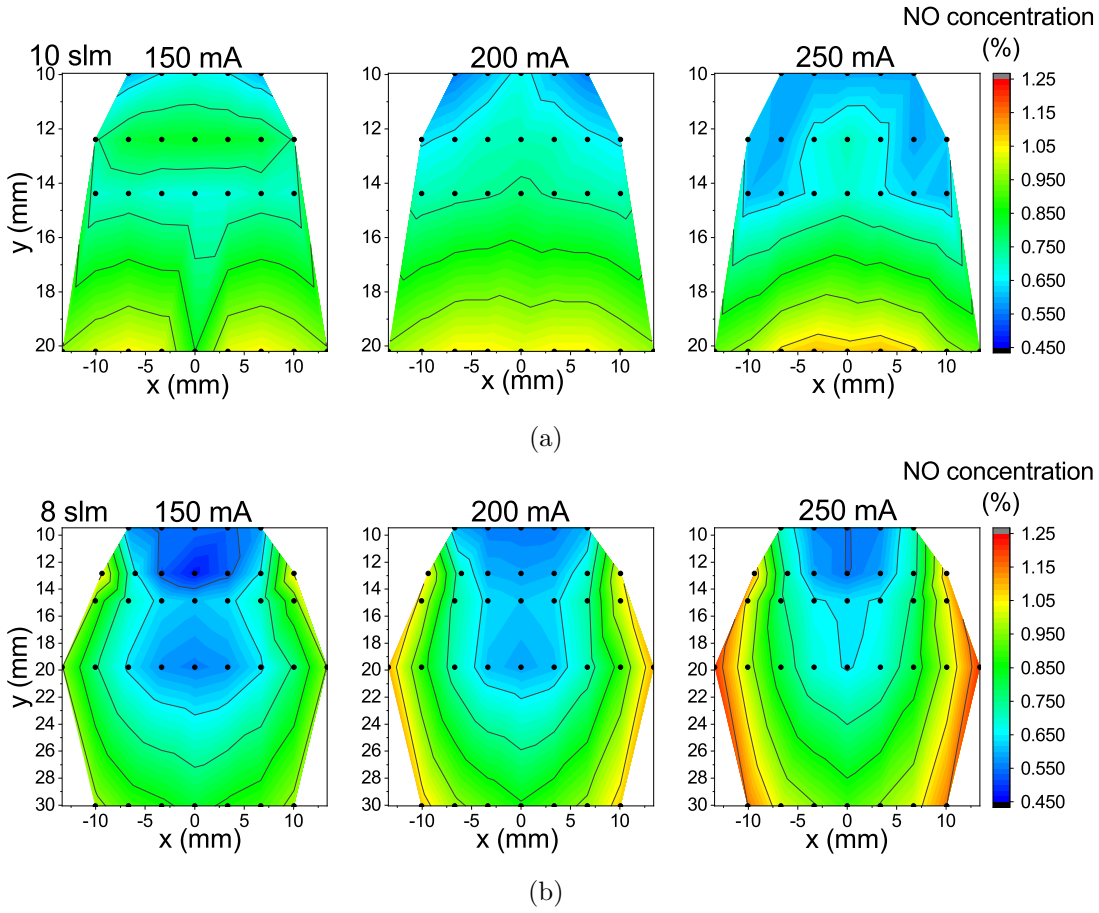

Figure 9: 2D vertical section of the NO(X) concentration distribution in the in the plasma afterglow at 10 slm (a) and 8 slm (b) with currents of either 150 mA, 200 mA or 250 mA. The data points are highlighted.

to expand towards the reactor walls. This generates a central region where T_{gas} is cooler than on the sides and limits the axial extension of the plasma. It is therefore observed that the T_{gas} distribution shows a rather high sensitivity to the input gas flow rate. With the lower input gas flow rate, the plasma region forms a column and remains confined along the center of the reactor, showing little difference within the region probed with the laser beam. Since, in this case, the plasma has a longer extension, additional measurements at 30 mm from the anode were acquired for 8 slm. Similarly to what is discussed with 10 slm, an elongation of the vertical plasma column is observed as the current increases, however, due to the constraints of the reactor design, probing further away from the anode was not possible.

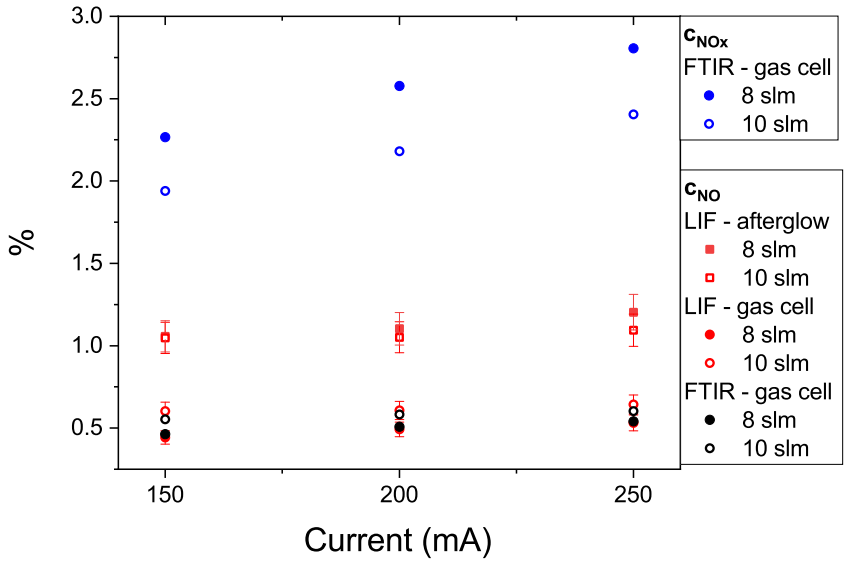

Figure 10: Maximum values for the LIF-measured NO(X) concentration in the afterglow compared with the FTIR-measured concentrations as a function of the current for 8 slm and 10 slm.

Similarly, the spatial evolution of c_{NO} is shown in figures 9a and 9b. In comparison with the 2D T_{gas} map, c_{NO} is higher in areas where T_{rot} is lower, reaching concentrations up to 1.1 %. The oxidation of NO into NO_2 is likely responsible for this trend as the rate for $NO + O \rightarrow NO_2$ becomes dominant in the temperature range between 1000 and 2000 K [11].

Figure 10 summarizes the maximum c_{NO} measured in each experimental condition. The relative error on c_{NO} is estimated to be of approximately 9 %. Such estimation is obtained by propagating the errors on the measurement of τ and E_{las} (the latter is estimated to be approximately 5 % of E_{las}). The instrumental error due to the ICCD measurement is considered to be negligible. These measurements are compared with the NO (c_{NO}) and the NO + NO_2 (c_{NO_x}) concentrations in the external gas cell measured with the FTIR. The statistical error associated with the FTIR concentrations is determined by repeating measurements for the same experimental conditions and is estimated to be of the order of 1 % of the measured values. To ensure a direct comparison between the c_{NO} measurements obtained with LIF and FTIR, additional LIF measurements were performed in the gas cell as well, resulting in comparable c_{NO} values as shown in figure 10. The maximum c_{NO} measured with LIF (which corresponds to regions where the fraction of NO(X) is higher) is consistently higher than the c_{NO} measured by FTIR. This is expected, as previously mentioned, due to the loss of NO caused by the Zeldovich back-reaction and by the conversion to NO_2. On the other hand, the NO + NO_2 concentration is higher,

suggesting that the conversion into NO_2 in the region probed with LIF is already significant.

Finally, the difference in NO and NO_2 concentrations measured with 8 and 10 slm is mostly associated with a higher specific energy input (SEI), defined as [34]

$$\mathrm{SEI} = \frac{P_P}{\text{gas flow rate} \cdot (1/22.4)(\mathrm{mol/L})}, \quad (16)$$

where P_P is the plasma power. This can be observed in figure 11 where the NO and NO_2 concentrations measured at 8 slm and 10 slm show a similar dependency on the SEI.

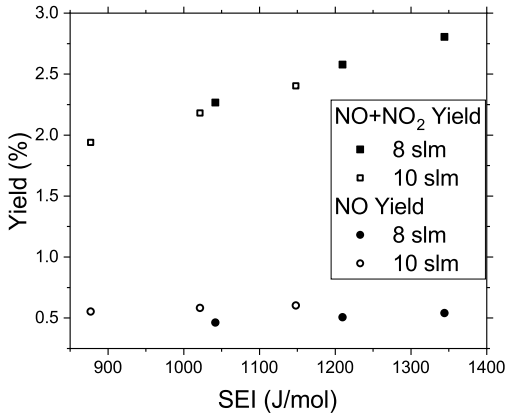

Figure 11: FTIR-measured concentrations as a function of the specific energy input (SEI) for 8 slm and 10 slm.

5 Conclusions

This work proposes the use of a method for the determination of the NO(X, $v = 0$) rotational temperature T_{rot} based on the line ratio between the $J = 33.5$ and the $J = 21.5$ LIF peaks, which is compatible with atmospheric plasmas where a high absorbance can prevent the use of more well-established methods. The $J_{33.5}/J_{21.5}$ line ratio is studied with LIFBASE and shown to be a monotonic function of T_{rot}. Such a method is then applied to study the afterglow of a gliding arc plasma operating at atmospheric pressure with N_2 and O_2 a few mm below the anode (i.e., the reactor outlet). The T_{rot} measured with such method are then used to determine, using the $J = 21.5$ LIF peak, the NO(X) concentration, measuring up to 1.2 % NO.

The NO(X) concentration measurements performed with LIF in the plasma afterglow are compared with the NO and NO_x concentrations detected at the exhaust with an FTIR. For each of the experimental conditions, the maximum LIF-measured concentration is observed to be (i) higher than the FTIR-measured c_{NO}, which is expected taking into account the NO losses due to the conversion into NO_2 and the back Zeldovich reaction, and (ii) lower than the FTIR-measured c_{NO_x}, which suggests that the conversion into NO_2 is already significant in the plasma afterglow region.

The obtained 2D spatial evolution of T_{rot} and of the NO(X) concentration highlights the NO(X) concentration being higher as T_{rot} decreases. The input gas flow rate is found to be a crucial parameter affecting the temperature gradients in the plasma afterglow region, which likely happens as a result of changes in the plasma shapes. This is particularly important as a fast T_{gas} quenching is known to inhibit the NO Zeldovich back-reaction.

6 Acknowledgements

This research is supported by the FNRS-FWO project "NITROPLASM", EOS O005118F. The authors thank Dr. Nikolay Britun (Nagoya University) for the critical reading of the manuscript.

References

(1) FAO *World fertilizer trends and outlook to 2022*; tech. rep.; FAO, 2019.

(2) Haber, F., *Thermodynamik Technischer Gasreaktionen*; Chemie Nobelpreisträger Schriften; Salzwasser-Verlag: 1905.

(3) Cherkasov, N.; Ibhadon, A.; Fitzpatrick, P. *Chem. Eng. Process* **2015**, *90*, 24–33.

(4) Clomburg, J. M.; Crumbley, A. M.; Gonzalez, R. *Science* **2017**, *355*, aag0804.

(5) IEA *Global CO_2 emissions in 2019*; tech. rep.; IEA, 2020.

(6) Rafiqul, I.; Weber, C.; Lehmann, B.; Voss, A. *Energy* **2005**, *30*, 2487–2504.

(7) Vervloessem, E.; Aghaei, M.; Jardali, F.; Hafezkhiabani, N.; Bogaerts, A. *ACS Sustain. Chem. Eng.* **2020**, *8*, 9711–9720.

(8) Bogaerts, A.; Neyts, E. C. *ACS Energy Letters* **2018**, *3*, 1013–1027.

(9) Jardali, F.; Van Alphen, S.; Creel, J.; Ahmadi Eshtehardi, H.; Axelsson, M.; Ingels, R.; Snyders, R.; Bogaerts, A. *Green Chem.* **2021**, *23*, 1748–1757.

(10) Van Alphen, S.; Ahmadi Eshtehardi, H.; O'Modhrain, C.; Bogaerts, J.; Van Poyer, H.; Creel, J.; Delplancke, M.-P.; Snyders, R.; Bogaerts, A. *Chem. Eng. J.* **2022**, *443*, 136529.

(11) Tsonev, I.; O'Modhrain, C.; Bogaerts, A.; Gorbanev, Y. *ACS Sustainable Chem. Eng.* **2023**, *5*, 1888–1897.

(12) Van Alphen, S.; Jardali, F.; Creel, J.; Trenchev, G.; Snyders, R.; Bogaerts, A. *Sustainable Energy Fuels* **2021**, *5*, 1786–1800.

(13) Wang, W.; Patil, B.; Heijkers, S.; Hessel, V.; Bogaerts, A. *ChemSusChem* **2017**, *10*, 2145–2157.

(14) Gromov, M.; Leonova, K.; Geyter, N. D.; Morent, R.; Snyders, R.; Britun, N.; Nikiforov, A. *Plasma Sources Science and Technology* **2021**, *30*, 065024.

(15) Kronemayer, H.; Ifeacho, P.; Hecht, C.; Dreier, T.; Wiggers, H.; Schulz, C. *Appl. Phys. BB* **2007**, *88*, 373–377.

(16) Van Gessel, A. F. H.; Hrycak, B.; Jasiński, M.; Mizeraczyk, J.; van der Mullen, J. J. A. M.; Bruggeman, P. J. *Journal of Physics D: Applied Physics* **2013**, *46*, 095201.

(17) Iseni, S.; Zhang, S.; van Gessel, A. F. H.; Hofmann, S.; van Ham, B. T. J.; Reuter, S.; Weltmann, K. D.; Bruggeman, P. J. *New Journal of Physics* **2014**, *16*, 123011.

(18) Preissing, P.; Korolov, I.; Schulze, J.; der Gathen, V. S.-v.; Böke, M. *Plasma Sources Science and Technology* **2020**, *29*, 125001.

(19) Ramakers, M.; Medrano, J. A.; Trenchev, G.; Gallucci, F.; Bogaerts, A. *Plasma Sources Science and Technology* **2017**, *26*, 125002.

(20) Trenchev, G.; Kolev, S.; Bogaerts, A. *Plasma Sources Science and Technology* **2016**, *25*, 035014.

(21) Gröger, S.; Ramakers, M.; Hamme, M.; Medrano, J. A.; Bibinov, N.; Gallucci, F.; Bogaerts, A.; Awakowicz, P. *Journal of Physics D: Applied Physics* **2018**, *52*, 065201.

(22) Britun, N.; Minea, T.; Konstantinidis, S.; Snyders, . *Journal of Physics D: Applied Physics* **2014**, *47*, 224001.

(23) Mitchell, A. C. G.; Zemansky, M. W., *Resonance Radiation and Excited Atoms*; Cambridge University Press, London: 1971.

(24) Merienne, M. F.; Jenouvrier, A.; Coquart, B.; Lux, J. P. *J. Atmos. Chem.* **1997**, *27*, 219–232.

(25) Di Rosa, M. D.; Hanson, R. K. *J Quant Spectrosc Radiat Transf.* **1994**, *52*, 515–529.

(26) Luque, J.; Crosley, D. LIFBASE: Database and Spectral Simulation Program, version 2.1.1, 1999.

(27) Bass, H. E.; Hill, G. L. *The Journal of Chemical Physics* **2003**, *58*, 5179–5180.

(28) Samadi Bahnamiri, O.; Manaigo, F.; Chatterjee, A.; Snyders, R.; D'Isa, F. A.; Britun, N. *Journal of Applied Physics* **2023**, *133*, 113303.

(29) Settersten, T. B.; Patterson, B. D.; Gray, J. A. *The Journal of Chemical Physics* **2006**, *124*, 234308.

(30) Voráč, J.; Dvořák, P.; Procházka, V.; Ehlbeck, J.; Reuter, S. *Plasma Sources Sci Technol.* **2013**, *22*, 025016.

(31) Britun, N.; Gamaleev, V.; Hori, M. *Plasma Sources Science and Technology* **2021**, *30*, 08LT02.

(32) Britun, N., Unpublished data, 2023.

(33) Verbiezen, K.; Klein-Douwel, R.; van Vliet, A.; Donkerbroek, A.; Meerts, W.; Dam, N.; ter Meulen, J. *Proceedings of the Combustion Institute* **2007**, *31*, 765–773.

(34) Ivanov, V.; Paunska, T.; Lazarova, S.; Bogaerts, A.; Kolev, S. *Journal of CO2 Utilization* **2023**, *67*, 102300.